Dalton Transactions

An international journal of inorganic chemistry

Accepted Manuscript

This article can be cited before page numbers have been issued, to do this please use: R. Zarroug, B. Artetxe, B. Ayed, X. López, N. Ribeiro, I. Correia and J. C. Pessoa, *Dalton Trans.*, 2022, DOI: 10.1039/D2DT00690A.

Volume 46
Number 10
14 March 2017
Pages 3073-3412

Dalton Transactions

An international journal of inorganic chemistry

rsc.li/dalton

ISSN 0306-0012

ROYAL SOCIETY OF CHEMISTRY

COMMUNICATION
Douglas W. Stephen *et al.*
N-Heterocyclic carbene stabilized parent sulfenyl, selenenyl, and tellurenyl cations (XH^+, X = S, Se, Te)

ROYAL SOCIETY OF CHEMISTRY

rsc.li/dalton

View Article Online
DOI: 10.1039/D2DT00690A

New phosphotetradecavanadate hybrids: crystal structure, DFT analysis, stability and binding interactions with bio-macromolecules

Rim Zarroug[a,b], Beñat Artetxe[c], Brahim Ayed[a], Xavier López[d], Nádia Ribeiro,[e] Isabel Correia,[e] João Costa Pessoa*[e]

[a] *University of Monastir, Laboratory of Physico-chemistry of Materials LR01ES19, Faculty of Sciences of Monastir, Tunisia*

[b] *Department of chemistry, Faculty of Sciences, University of Gabes, Tunisia*

[c] *Departamento de Química Inorgánica, Facultad de Ciencia y Tecnología, Universidad del País Vasco UPV/EHU, 48080 Bilbao, Spain*

[d] *Universitat Rovira i Virgili, Departament de Química Física i Inorgànica, c/Marcel·lí Domingo 1, 43007 Tarragona, Spain*

[e] *Centro de Química Estrutural, Institute of Molecular Sciences and Departamento de Engenharia Química, Instituto Superior Técnico, Universidade de Lisboa, Av. Rovisco Pais, 1049-001 Lisboa, Portugal*

Abstract

Two novel bicapped Keggin polyoxidovanadates with organic cations, $(C_6H_8N)_5[H_4PV_{14}O_{42}]\cdot5H_2O$ (**1**) and $(C_6H_{14}N_4)_2(NH_4)[H_4PV_{14}O_{42}]\cdot11H_2O$ (**2**), ($PV_{14}O_{42}^{6-}$ = PV14, C_6H_7N = 3-picoline and $C_6H_{12}N_4$ = methenamine) were synthesized. These compounds were isolated and characterized in the solid state and in solution by elemental analysis, powder X-Ray diffraction, FTIR, UV-Vis, ^{51}V, ^{31}P, ^{13}C and ^{1}H NMR, and fluorescence spectroscopies. Further confirmation of the PV14 structures was obtained by single-crystal X-ray diffraction studies of **1** and **2**. The Hirshfeld surface analysis was evaluated to confirm that within the intermolecular interactions occurring in the two crystals the O⋯H/H⋯O, O⋯O and H⋯H interactions dominate. The protonation and one-electron reduction of the PV14 moiety was also analysed by means of DFT calculations; besides confirming the protonation sites and correctly predicting the pK_a values, the DFT results indicate that molecular reduction is energetically more favourable in protonated PV14 anions. Upon addition of PV14 anions to bovine serum albumin (BSA) up to 1:1 PV14:BSA ratio, the fluorescence decreased by 45% for **1** and 45% for **2**, indicating that interaction of vanadium-containing species with this protein take place; log(K_{SV}) values of ca. 5.5 were obtained in both systems. Upon addition of **1** or **2** to solutions of Calf-Thymus DNA (ctDNA)

DOI: 10.1039/D2DT00690A

changes were observed in the UV-Vis absorption and circular dichroism spectra. The significance of the changes observed are discussed considering the several V-containing species that form in solution.

Keywords: Bi-capped Keggin polyoxidovanadate, X-ray Diffraction, Hirschfield surfaces, DNA interaction, BSA binding, DFT calculations

Introduction

Polyoxidometalates (POMs) are transition metal oxides where metal atoms usually present their highest oxidation states (usually group 5 or 6 in the periodic table, such as V^V, Nb^V, Ta^V, Mo^{VI} and W^{VI}) by their binding to oxygen atoms, forming clusters with well-defined structures with the metal ion, and its nearest coordination sphere acting as a polyhedral building block.[1, 2] POMs[3] have attracted increasing attention due to their potential applications in catalysis,[4-11] electrochemical energy storage and conversion[12-14] and magnetism,[15, 16] as well as in several areas of material, medicinal and environmental sciences.[17-25] The size, structural shapes and modifiable load densities of POMs often yield unexpected and interesting behaviours, allowing them to display different physical and chemical properties compared to traditional metal oxides.[26, 27]

Polyoxidovanadates (POVs) are a relevant subfamily of POMs. The diverse coordination geometries and cluster sizes observed in such vanadium oxide polyhedral shapes and the different oxidation states that vanadium centres can adopt give rise to a great variety of distinct architectures[28] that have attracted increasing attention. In contrast to molybdates and tungstates, which are typically based on $[MoO_6]$/$[WO_6]$ octahedra as fundamental building units, POVs show more structural flexibility, featuring tetrahedral $[VO_4]$, square pyramidal $[VO_5]$ and octahedral $[VO_6]$ units.[14, 29-33] However, this versatility also facilitates structural rearrangements which need to be considered when deploying POVs for prospective applications.[22, 24, 29, 33, 34] In addition, POVs are often designated as being “less stable” than tungstates and molybdates, which is most likely due to a combination of their structural flexibility, complex protonation chemistry, possible hydrolysis and redox activity.[29, 31, 33]

It is well known that vanadate ions and vanadium compounds inhibit or stimulate the activity of many enzymes.[24, 25, 35-40] Namely, vanadate is well known to be an inhibitor of Na^+/K^+-ATPase[37, 41-43] and POVs have been discussed to have ion pumps such as Na^+/K^+-ATPase and Ca^{2+}-ATPase as one of the possible targets in their biological action.[24, 44-46] Vanadate(V) anions

View Article Online
DOI: 10.1039/D2DT00690A

show many similarities with phosphate and are known to inhibit or stimulate several enzymes, namely phosphatases and kinases.[35, 39]

Much attention has been paid to the design and synthesis of organic-inorganic hybrids, metal-organic frameworks or associations through the modification of metal oxides by organic molecules, or simply with organic molecules acting as counter-ions, leading to new materials. Hybrid inorganic-organic materials are prepared by combining organic and inorganic building blocks.[47] The nature of the links between the organic and inorganic phases was used to divide them into two distinct classes: in Class I, only electrostatic interactions, hydrogen bonds or van der Waals interactions are involved in the binding of the organic and inorganic moieties; in Class II, organic and inorganic groups are bound together by strong chemical covalent or iono-covalent bonds,[48] and POVs may be considered good candidates to produce both Class I and Class II type materials.[11, 49, 50]

In this work, we selected bicapped Keggin phosphotetradecavanadates ($PV_{14}O_{42}^{6-}$ = PV14) anions as inorganic building blocks and describe the synthesis, characterization and crystal structure of two organic-inorganic hybrid compounds, namely $(C_6H_8N)_5[H_4PV_{14}O_{42}]\cdot 5H_2O$ (**1**) and $(C_6H_{14}N_4)_2(NH_4)[H_4PV_{14}O_{42}]\cdot 11H_2O$ (**2**), where C_6H_7N = 3-picoline and $C_6H_{12}N_4$ = methenamine = HMTA. Additionally, Hirshfeld surface analysis of these POVs were obtained to analyse and study the nature of contacts in the crystal packing, and DFT studies to evaluate the relative stability of H_nPV14 species and their propensity to reduction and interaction with other molecules. Importantly, we also check the stability of the PV14 anions in aqueous solution at pH~7 and find that these anions are kinetically less stable than decavanadates. Moreover, the lower is their concentration the faster they decompose. This is relevant in evaluating biological data involving PV14 anions as at concentrations below ca. 50 μM these become extensively hydrolysed as soon as dissolved in solutions at pH ~7. We also found that PV14 interacts with bovine serum albumin (BSA); at low concentrations of the polyanions, these decompose and the several vanadium containing species formed may also bind to the protein.

Results and Discussion

Description of structures

To precipitate and isolate the phosphotetradecavanadate anions, the synthetic approach used in this study consisted in a one-pot strategy in which a unit of POV assembles around a central

View Article Online
DOI: 10.1039/D2DT00690A

phosphate molecule by acidifying an aqueous vanadate solution with dilute phosphoric acid. One of the objectives of the present work was to better understand supra-molecular interactions in PV14 anions; thus we introduced 3-picoline organic cations as counter-ions in **1** (Fig. 1) and HMTA (hexamethylenetetraamine, methenamine) organic cations in **2** (Fig. 2), and were successful in obtaining crystals suitable for single-crystal X-Ray diffraction (SC-XRD) studies. To favour the formation of crystalline materials, organic cations were used in five-fold excess. The synthetic procedure allowed us to isolate compounds **1** and **2** within crystallization times of 4 h and 7 h, respectively, in yields of more than 90% (based on V). Structural analysis of the diffraction data (Table S1) showed that the main inorganic construction units in **1** and **2** are the heteropolyoxidovanadate clusters $[H_nPV_{14}O_{42}]^{(9-n)-}$.

The main structural compensation results from the incorporation of two oxidovanadium(V) fragments[51], $[V{=}O]^{3+}$, that are linked to vacant coordination sites formed by four O-oxido atoms on the cluster surface, thus globally reducing the negative charge of the cluster. Secondary charge compensation is obtained by the protonation of surface O-atoms, resulting in the final cluster formula $[H_nPV_{14}O_{42}]^{(9-n)-}$.

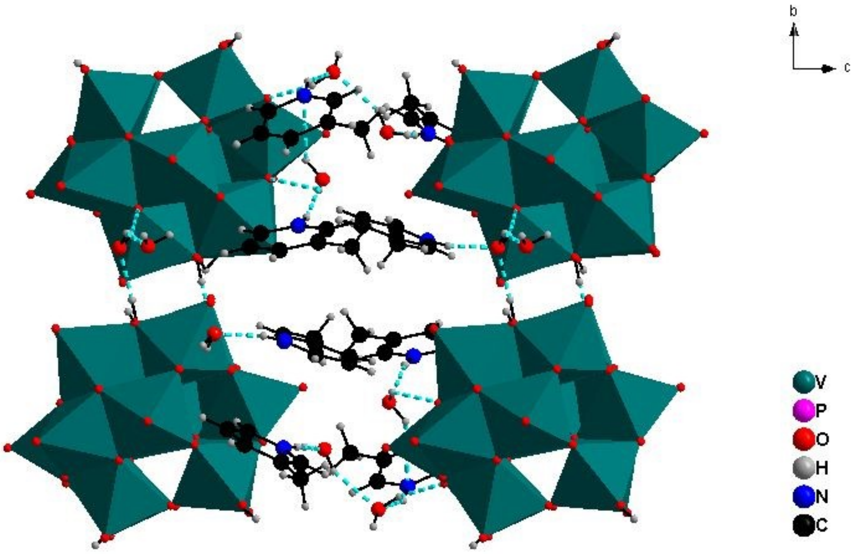

Fig. 1 Hydrogen bonding around water molecules, organic cations and terminal O-atoms of polyanions of **1**.

As mentioned earlier, the PV14 cluster is structurally closely linked to the Keggin archetypal cluster. The centre of the cluster is occupied by a tetrahedral site, in this case a phosphate PO_4^{3-} anion. Each O-atom of the phosphate anion acts as a central anchor for a triad $[V_3O_{13}]$, where three vanadium(V) centres are connected in a symmetrical trigonal construction unit C_{3v}; each V center is connected to neighbouring groups by a μ_2-oxido ligand at distances: d(V–O) = 1.6–2.3 Å. In addition, each V-centre has an O-oxido terminal ligand with the typically short V-O distances close to 1.6 Å.

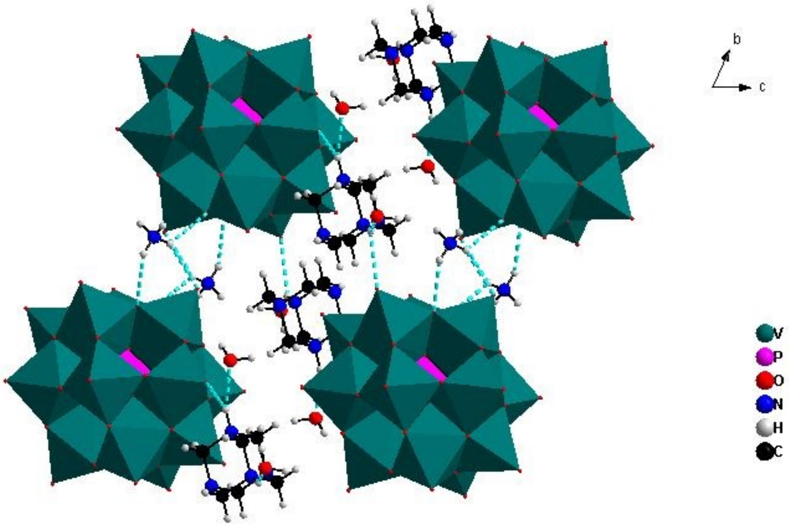

Fig. 2 Hydrogen bonding around water molecules, organic cations, ammonium cation and terminal O-atoms of polyanions of **2**.

Selected bond distances and angles for **1** and **2** can be found in Tables S2-S5 (ESI). It should be noted that the 12 vanadium centres that form the envelope of the Keggin-based cluster form six octahedral [VO_6] moieties, while the additional oxidovanadium(V) halves adopt a square-pyramidal [VO_5] coordination mode.[52, 53] Theoretical analysis of the structure of the clusters using Bond Valence Sum calculations (BVS) and UV-Vis spectroscopy confirms that all vanadium centres are fully oxidized V^V units. In addition, the BVS calculations allowed us to locate the protonation sites and thoroughly analyse the metal-oxygen bond lengths based on the SC-XRD analysis. Analysis of the crystal structure of **1** and **2** using a combination of Hirshfeld analysis, manual structural analysis and BVS calculations allowed us to identify a range of highly directed intermolecular interactions which are considered to contribute significantly to the packaging of units in the crystalline network in both compounds. Using a combination of structural analysis and theoretical BVS calculations, we were able to identify four protonation sites on the PV14 clusters of **1** and **2**. Four kinds of O-atoms exist in the PV14 clusters according to the manner of oxygen binding (Tables S2-S4, ESI): there are (i) 14 terminal O-atoms which are only bonded to one V atom, with V-O distances in the range 1.594-1.614 Å in **1** and 1.578-

1.598 Å in **2**; (ii) 16 O-atoms which are shared by two V-atoms, with V-O distances varying from 1.702 to 2.045 Å in **1** and from 1.744 to 1.933 Å in **2**; (iii) 8 O-atoms which are combined with three V-atoms with V-O distances varying from 1.822 to 2.075 Å in **1** and from 1.822 to 2.036 Å in **2**; (iv) 4 O-atoms which are bound to one P-atom and three V-atoms, with V-O distances varying from 2.323 and 2.43 Å in **1** and from 2.376 and 2.470 Å in **2**.

Comparison of the two PV14 clusters of **1** and **2** of α-Keggin type shows that the central PO_4 tetrahedron differs. In **1** the P-O distances vary from 1.532(4) to 1.543(4) Å and the angles are between 108.1(2)° and 110.7(2)° (Tables S2 and S3, ESI), indicating normal tetrahedral phosphorus, while in **2** the central PO_4 tetrahedron has a type of disorder, with half-occupancy of the O-atom sites, akin of that noted in some Keggin-type $[XM_{12}O_{40}]^{n-}$ heteropolyanions, indicated by Evans and Pope as being the result of a crystallographic disorder.[54] The P-O distances vary from 1.479(11) to 1.566 (10) Å and the angles are between 105.9(6) and 113.0 (6) (Tables S4 and S5, ESI), corresponding to distorted phosphorus tetrahedrons.

The bond length and bond-angle distortion indices (ID) were calculated following the Baur method.[55] The parameters obtained are in the ranges of 0.086–0.166 for ID (V-O) and 0.050–0.333 for ID (O-V-O) for **1**, and in the ranges of 0.085–0.145 for ID (V-O) and 0.189–0.333 for ID (O-V-O) for **2**. The bond distances within the POV unit of these hybrid compounds are in agreement with the values reported for Keggin-type compounds.[8]

BVS calculations using the Brown and Altermatt method[56] revealed that all the vanadium atoms have valence sums ranging from 4.370 to 5.139 (in **1**) and from 4.941 to 5.183 (in **2**), with an average value of 5.02 for **1** and **2**, close to the ideal value of 5 for V. The bond valences of phosphorus atoms are 5.28 (**1**) and 5.12 (**2**). The bond valences of O-atoms in the polyanion are in the range 1.654–1.754 valence units for terminal O-atoms and 1.805–2.056 valence units for bridging O-atoms, except 1.25 for O(8), 1.264 for O(13), 1.224 for O(24) and 1.341 for O(29) in **1**, and also 1.496 for (O8) and 1.495 for O(3) in **2**, indicating that in each compound the clusters are protonated and the protonation O-atoms are O(8), O(13), O(24) and O(29) for **1** and O (11) and O(13) for **2**.

In the packing structure for both compounds, the variety of hydrogen bonds O–H···O, O_W–H ···O $_W$, N-H···O_W, O_W–H···N and O_W–H···O enhance the stability of the crystalline building blocks. The geometric characteristics of the hydrogen bonds are described in Tables S6 and S7 (ESI).

The asymmetric unit of $(C_6H_8N)_5[H_4PV_{14}O_{42}]\cdot5H_2O$ is composed of one Keggin type $[H_4PV_{14}O_{42}]^{5-}$, five 3-picoline cations $[C_6H_8N]^+$ and water molecules. The structure of **2** is based on one Keggin cluster, two H_2HMTA^{2+} cations, ammonium cation and eleven water molecules. The structural analysis revealed that the crystal packing in both compounds exhibits a network of N-H···O, O_w-H···O and O-H···O hydrogen bonds involving water molecules and organic molecules as well as van der Waals interactions for the connections between the organic moieties. The IR spectra distinguished bands of organic cations, PV14 moieties and water molecules. Spectroscopic studies of the interaction of these compounds with BSA (and also with ctDNA) confirmed the interaction of **1** and **2** with these biomolecules (see below).

In compound **1**, each anionic unit $[H_4PV_{14}O_{42}]^{5-}$ is associated to five 3-picoline cations and five molecules of water, the hydrogen bonds directly linking PV14 anions by water molecules in a zigzag chain, which are then woven into a bi-dimensional network by hydrogen bonds bridged by water molecules, and one of the H-atom bound to O(13) and another of O(24). The adjacent inorganic-organic chains are also joined to produce a 3D-supramolecular architecture through hydrogen bonds and Van der Waals interactions between the 3-picoline cations, water molecules and polyoxido anions (Fig. 1).

In compound **2**, each anionic unit $[H_4PV_{14}O_{42}]^{5-}$ is associated to two H_2HMTA^{2+} cations, one NH_4^+ cation and 11 molecules of water. Each polyanion PV14 is bound by short hydrogen bonds to the ammonium cations and H_2HMTA^{2+} by O-atoms with distances N24···O13, N24···O8 ^{iv}, N24···O19 ^{v}, N3···O16 and N4···O15’, respectively of 2.896, 3.135, 3.003, 3.036 and 3.211 Å, which exhibits an interesting wavelike 2D network in the crystal structure. In addition, the cation is connected to water molecules through hydrogen-bonding interactions with N3···OW3 distance of 2.805 Å, as well as a N4···OW5 distance of 3.047 Å (Fig. 2). These hydrogen bonds hold the components together in a three-dimensional network and make the crystalline structure of the compound stable enough for crystallization to take place.

Thermogravimetric analysis

The thermal stability of the compounds was studied and TGA profiles are presented in the ESI section. The samples analysed are not the same as the ones used for SC-XRD studies. However, for compound **1** the profile obtained is consistent with (i) the loss of five water molecules (*ca.* 4%), (ii) the loss of the organic moieties and the O atom in two steps (*ca.* 36%) and (iii) V_2O_5 as the final product (*ca.* 65%); this residue corresponds to a %V of 36 in the initial sample, coinciding with the expected %V (36.0%). For complex **2** the data is also globally consistent with the structure solved by SC-XRD: it indicates 9% mass loss between 30 – 175 ºC (*ca.* 10.8 H_2O molecules) and three steps corresponding to an overall mass loss of 31% between 145 - 600ºC. The final mass of the residue corresponds to 60% of the initial mass, which is lower than the expected (67%), but as mentioned above, the solid used was from a different batch.

FTIR characterization of 1 and 2

The FTIR spectra of the two compounds in KBr pressed pellets are depicted in (Fig. S1, ESI).

The spectra of **1** and **2** display the stretching of the terminal $V=O_t$ bonds (Table 1) and bands in the range 500-1000 cm^{-1} are partly due to several types of V-O vibrations. Those at about 879 and 743 cm^{-1} are assigned to the asymmetric stretching vibration of $V–O_{b/c}–V$. The bands between 596 and 594 cm^{-1} can be assigned to the (V–O–V) remaining stretchings, but 3-picoline has also bands in this region.[57] The stretching bands of the P–O bond are assigned at 1063 cm^{-1} and 1060 cm^{-1} respectively for **1** and **2**.[58, 59] The lattice water absorption bands centered at 3429 cm^{-1} and 3405 cm^{-1} are more intense in **2** than in **1**, in agreement with their relative water content.

The peaks at 3059, 1672, 1560, 1471 and 1426 cm^{-1} in **1** may be regarded as characteristic of the 3-picoline moieties,[60, 61] and the bands at 3400, 3196, 2268, 1615, 1450 and 1263 cm^{-1} in **2** are assigned to the various vibrational modes of the HMTA cations.[62, 63]. These results are consistent with the SC-XRD data.

Table 1 Infrared absorptions and tentative assignments for compounds **1** and **2**

Compound **1**

Frequency / cm^{-1}	Assignment	Frequency / cm^{-1}	Assignment
3429	ν(O-H)	1426	δ(N-H)
3059	ν(N-H)	1063	ν(P-O)
1672	ν(C=C)	938	$\nu(V=O_t)$
1560	ν(N=C)	761; 798	$\nu_{as}(V\text{-}O_{b/c})$
1471	δ(C-H)	596	$\nu_s(V\text{-}O_{b/c})$

Compound **2**

Frequency / cm^{-1}	Assignment	Frequency / cm^{-1}	Assignment
3404	ν(O-H)	1263	δ(N-C)
3400; 3196	ν(N-H)	1060	ν(P-O)

View Article Online
DOI: 10.1039/D2DT00690A

2268	ν(N-C)	936; 860	ν(V=O$_t$)
1615	δ(O-H)	752; 797	ν$_{as}$(V-O$_{b/c}$)
1450	δ(N-H)	594	ν$_s$(V-O$_{b/c}$)

X-Ray Powder Diffraction Pattern of compounds 1 and 2

The purity and crystalline nature of powders of **1** and **2** were confirmed by comparison using the Origin software,[64] of the experimental diffractograms (λ_{Mo} (Kα1) = 0.71073Å) with the calculated diffractograms from SC-XRD data (see below), obtained using the VESTA program.[65] The superposition of the two diffractograms (Fig. S3, ESI) and their very good correspondence confirms that the two synthesized powders in fact correspond to compounds **1** and **2**, without any significant presence of other phases.

Nuclear Magnetic Resonance (NMR)

Compounds **1** and **2** were characterized in aqueous solution by ^{51}V NMR spectroscopy and some of the spectra measured with samples of compound **2** are depicted in Fig. 3.Several other ^{51}V NMR, ^{1}H NMR, ^{13}C NMR and ^{31}P NMR spectra are depicted in Figs. S24 to S38.

In the ^{51}V NMR spectrum of compound **2** recorded at pH 2.3, three peaks at –530, –584 and –596 ppm correspond to the ^{51}V NMR chemical shifts (δ_V) of the partially protonated anions $[H_4PV_{14}O_{42}]^{5-}$ and $[H_5PV_{14}O_{42}]^{4-}$,[66] while one band at δ_V = –542 ppm is due to some amount of $V^VO_2^+$ (V_1, monovanadate) possibly formed during dissolution of **2**; similar spectra were measured for PV14 anions by Friedl *et al.* at the same pH[67] in a solution also containing 0.05 M H_3PO_4. Noteworthy, after 24 h the ^{51}V NMR spectra measured did not change significantly, confirming the stability of the PV14 cluster in these conditions (pH = 2.3) for at least 24 h. Similar results were obtained for compound **1** at pH = 2.75 (Fig. S24). In contrast, in the spectra measured with compound **2** at higher pH with freshly prepared solutions, new peaks were observed due to partial hydrolysis of the PV14 anions. At pH 5.6 peaks were observed at δ_V values of –520, –570 and –588 ppm, mainly due to $[H_3PV_{14}O_{42}]^{6-}$, and a small sharp peak at –559 ppm due to V_1. At pH 7.2 peaks were observed at δ_V values of –512, –563 and –582 due to PV14 anions, and in some experiments at –558, –571 and –575 ppm due to V_1, V_2 (divanadate) and V_4 (tetravanadate), respectively,[66] which increase intensity after 24 h. Although in true equilibrium conditions PV14 anions should not exist at pH > 4.5 (see Figs.

S11-S16, ESI), these POVs are kinetically stable for relatively short periods and may persist for several hours depending on pH and total V and P concentrations.

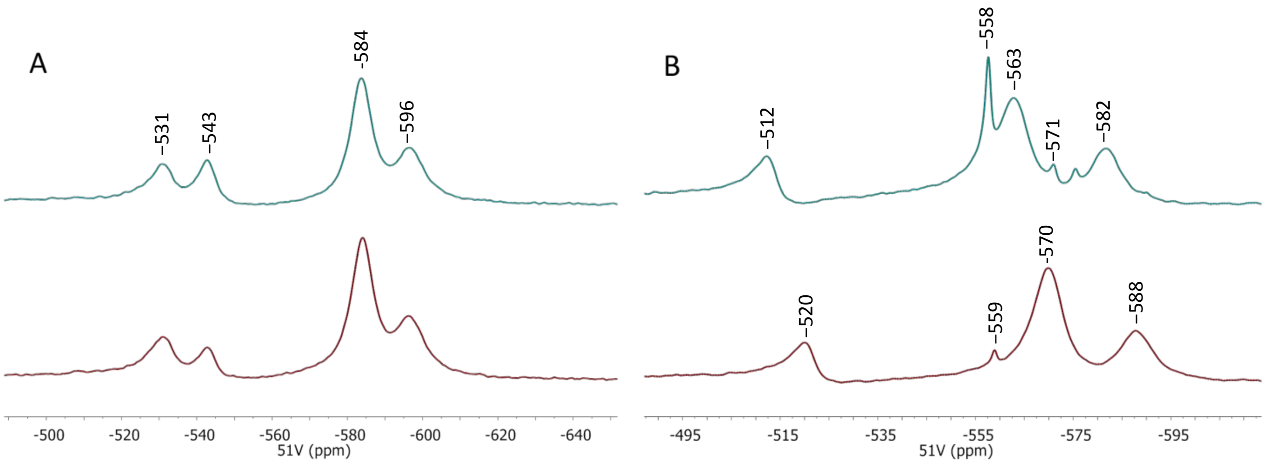

Fig. 3 ^{51}V NMR spectra recorded for 2 mM of compound **2** in water **(A)** at pH = 2.3, shortly after solution preparation (bottom, reddish curve) and after ca. 24 h (top, green curve); **(B)** 1 mM solutions of compound **2** in Hepes buffer at pH = 5.6 (bottom line) and at pH = 7.2 (top line). The pH was adjusted with a NaOH (4 M) solution and the spectra were recorded a few minutes after preparation of each solution.

Several studies have addressed ^{31}P NMR spectra of POMs.[29 66 68 69] The ^{31}P NMR spectrum of compounds **1** and **2** at pH = 2.75 are depicted in Figs. S27 and S35, respectively. In the case of **1** two peaks are detected at -0.05 ppm (major) and -0.16 ppm (minor), δ_P values being given relatively to the reference used (see experimental). In the case of **2** only one peak is detected at t = 0 h (at -0.62 ppm) immediately after preparation, and after 24 h the ^{31}P NMR spectrum shows a peak at -0.68 ppm, indicating a change in the environment of the phosphorous atom. The peaks at ca. -0.6 – -0.7 agree with those reported for PV14 compounds by Selling et al.[66] The ^{1}H NMR (Figs S30 and S37) and ^{13}C NMR (Figs S31 and S38) spectra of compounds **1** and **2** at pH = 2.75 present the pattern expected for the organic cations present in the corresponding solutions.

The ^{31}P NMR spectra of compounds **1** and **2** at pH = 7.1 in Hepes buffer are depicted in Figs. S28 and S36, respectively, up to 24 h of preparation of the solutions. In all spectra only one peak is detected. At t = 0 h in both cases the chemical shift is -0.75 ppm; while with compound **1** this is maintained up to 24 h, in the case of **2** the chemical shift progressively shifts to -0.85 ppm at t = 24 h.

View Article Online
DOI: 10.1039/D2DT00690A

To confirm that PV14 compounds may interact with BSA, several ^{51}V NMR and ^{31}P NMR spectra were recorded with solutions of compounds **1** and **2** at pH = 7.1 in Hepes buffer up to 24 h (40 h in some cases) of preparation of the samples. These contained a BSA:PV14 molar ratio of 0.3. In both cases the ^{51}V NMR spectra, Fig. S26a (case of **1**) and S34a (case of **2**), depict very broad bands suggesting interaction of both compounds with BSA. At t = 0 h a peak corresponding to V_1 is detected. With time, up to 24 h peaks corresponding to V_2 and V_4 show up, these being more intense in the case of compound **2**. The ^{51}V NMR spectra recorded with samples of **1** and **2** with a BSA:PV14] molar ratio of 1.6 (Fig. S26b, compound **1**) or 1.3 (Fig. S34b, compound **2**), yielded similar results but the NMR bands are broader and only V_1 is clearly detected.

In these ^{51}V NMR spectra of solutions containing PV14 compounds and BSA, because the bands are very broad, no clear peaks corresponding to the polyanions bound to BSA could be detected, and only relatively sharp bands of probably non-bound V_1, V_2 and V_4 could be identified (some vanadate-phosphate species may also be detected in the δV range -520 to -600 ppm[29]). Therefore no conclusion clarifying which vanadium containing species are bound to BSA, or if the integrity of the PV14 anions is maintained or not, cannot be taken. At much lower concentrations of the polyanions the driving force for their decomposition is greater, as may be inferred from the species distribution diagrams of Figs. S11-S16. We therefore expect quite extensive hydrolysis at concentrations lower than ca. 100 µM, yielding V_1, V_2 (and V_4). Monovanadate is known to bind BSA,[70] and at very low concentrations and high BSA:PV14 molar ratios we would predict mainly V_1 to be bound to the protein. However, the available techniques do not allow to confirm this.

Because PV14 anions are not stable for pH > 4.5,[29, 66] particularly for low vanadium concentrations, any effects detected in biologically relevant conditions, namely low total V concentration and in the presence of potential binders of vanadium, cannot be simply attributed to PV14 anions. We did several experiments (see below and ESI section) testing the binding of compound **2** to DNA and BSA. Our data indicate that the PV14 anions may bind to these macromolecules, but several species may be responsible for the effects detected in biologically relevant conditions, namely low total V concentration and in the presence of potential binders of vanadium; these effects cannot be simply attributed to PV14 anions (see also Figs. S16a-f, ESI section).

Hirshfeld Surface Analysis

View Article Online
DOI: 10.1039/D2DT00690A

Hirshfeld surfaces and 2D fingerprint plots[71] were generated in order to visualize the intermolecular interactions and access quantitatively their relative contributions. The Hirshfeld surface enclosing a molecule is defined by a set of points in 3D space where the contribution to the electron density from the molecule of interest is equal to the contribution from all other molecules. Hirshfeld surfaces are constructed based on electron distribution calculated as the sum of spherical atom electron densities. The Hirshfeld surface was carried out and the 2D Finger Print plots were plotted using Crystal Explorer 3.0.[72] This method was created for the two compounds with normalized contact distance (dnorm) calculated using the following equation:[73]

$$dnorm = \frac{di - rivdw}{rivdW} + \frac{de - revdW}{revdW}$$

Where “de” is the distance from the point to the nearest nucleus external to the surface, “di” is the distance to the nearest nucleus internal to the surface and “vdW” is the van der Waals radii of the atom. The dnorm surface is mapped on the Hirshfeld surface with blue, white or red colors. The dnorm value is negative (red) when intermolecular contacts are shorter than the van der Waals radii, and the dnorm value is positive (blue) when longer. The dnorm value of the white zones is zero and represents contacts equal to the van der Waals radius. In Fig. S4 (ESI), these Hirshfeld surfaces are mapped over the ranges –0.717 (red) to 1.467 (blue) for **1** and –1.091 (red) to 2.088 (blue) for **2**.

The analysis of the Hirshfeld data reveals the electrostatic complementarity between the electro-negative (red) patches around the O-atoms of the cations and polyoxovanadate molecules; also the electropositive (blue) regions around the nitrogen and carbon atoms of the cations and polyoxovanadate moieties.

Quantitative analysis (fingerprint plots) of the relative contribution of the variable forces responsible for the solid-state structure reveals that the contribution of hydrogen bonds (O···H/ H···O close contacts) for **1** and **2** are 54.8% and 41.8%, respectively, and appears to be a major attractive contributor in the crystal packing (Figs. S4-S6, ESI**)**. The major input of the repulsion forces (H···H and O···O) for compound **1** and (O···O) for compound **2** between the water and polyoxovanadate are 17.5% and 13.8% and 45.7%, respectively (Figs. S4-S6, ESI**)**. The individual intermolecular interactions and the quantitative contributions are displayed by the d_{norm} surfaces shown in (Fig. S4, ESI). Globally the Hirshfeld surface analysis gives a quite

View Article Online
DOI: 10.1039/D2DT00690A

complete understanding of the intermolecular interactions in the crystal. The O···H/H···O, O···O and H···H interactions are dominant, but both hydrogen bonding and van der Waals interactions play the main roles in the crystal packing of the two compounds.

UV-Vis spectra

Several UV-Vis spectra were recorded with time for solutions of compound **2** in Hepes buffer at pH ~7.0 and Figs. S7a-d (ESI) depict spectra for total concentrations of 5, 12, 20 and 100 μM. It may be noticed that all spectra significantly change with time, confirming that compound **2**, as other PV14 polyanions, is not stable at this pH. It should also be highlighted that, as expected, the lower the total concentration of **2**, the faster the changes take place, due to hydrolysis of the PV14 polyanion.

Each possible decomposition species of PV14 anions contributes differently to the UV spectra, some with opposite trends in absorbance values. In our systems at pH = 7, in what we consider time = 0 h, the PV14 anions have already decomposed significantly, and it is not easily feasible to quantify kinetics of decomposition as the several processes occurring are yielding opposite trends in the change of UV absorption. The maximum concentrations studied were 100 μM, and decomposition is about twice faster at 50 μM; globally absorption increases in both cases. The trend of change of absorption changes for lower concentrations (absorption decreases), at 5 μM being around twice faster than at 20 μM.

Fig. S8 (ESI) depicts changes observed in the UV spectra of BSA (49.1 μM) in Hepes buffer at pH = 7; the minor changes noticed with time up to 24 h show no clear trend and probably are not due to any modification of BSA. Fig. S9 (ESI) depicts changes observed in the UV spectra of compound **2** (49.1 μM) in similar conditions at pH = 7; quite significant changes take place with time up to 24 h, the increase of absorption up to 6 h being 0.199. Fig. S10 (ESI) depicts changes observed in the UV spectra of a solution containing compound **2** (49.1 μM) and BSA (100 μM) in Hepes buffer at pH = 7; some changes also take place with time up to 24 h, and the increase of absorption up to 6 h was 0.125 (Fig. S10, ESI), mostly due to hydrolysis of the PV14 polyanion. Noteworthy, this change in absorption is much lower when BSA was present in solution (0.125 *vs*. 0.199), suggesting that PV14 binds to BSA, delaying its hydrolysis at pH = 7. Notwithstanding, clear changes are observed with time in Fig. S10 (ESI), indicating progressive hydrolysis of the PV14 polyanion. At lower concentrations of PV14 (< 49 μM), even in the presence of BSA, hydrolysis probably proceeds faster.

View Article Online
DOI: 10.1039/D2DT00690A

Fluorescence spectra

Assessing BSA binding by steady-state fluorescence spectroscopy

Human serum albumin (HSA) is one of the major carrier proteins in human plasma, and BSA the most abundant in bovine plasma. The capacity of albumin to bind and transport a large variety of compounds results in its prevailing role in drug pharmacokinetics and pharmacodynamics, and drug bioavailability *in vivo*. BSA is composed by a single chain of 583 residues and a molecular weight of about 66430 g mol^{-1},[74, 75] having a multi-domain structure that may account for its remarkable ligand binding properties.[74, 76-78] The intrinsic fluorescence of albumins is due to their tryptophan (Trp), phenyl-alanine and tyrosine residues, of which Trp emission is predominant and can be selectively excited at 295 nm. BSA has two Trp residues: Trp-134 located on the surface of sub-domain IB and Trp-212 located within a hydrophobic binding pocket in sub-domain IIA. Emission from Trp-212 is very sensitive to changes in the environment around this residue, due to drug binding or to structural alterations of the protein. Trp-212 emission can thus be used as an intrinsic structural probe for drug binding and its quenching is a good indicator of binding of molecules to BSA, particularly those near the hydrophobic pocket of sub-domain IIA.[79]

The binding of **1** and **2** to BSA was studied by steady-state fluorescence spectroscopy. Both compounds are not emissive in Hepes buffer solution (λ_{exc} = 295 nm), so BSA fluorescence emission was measured in the absence and in the presence of increasing amounts of **1** and **2**. Figs. 4 and S17 (ESI) depict the results, and the Stern–Volmer quenching constants (K_{sv}) calculated[80] are included in Table 2.

Compounds **1** and **2** exert a moderate quenching effect on Trp-212 fluorescence, with a decrease of *ca.* 45% for the higher molar ratio of **1**:BSA used (0.94), Fig. 4) and a decrease of *ca.* 52% for the higher molar ratio of **1**:BSA used (2.02, Fig. S17), with no shift of the emission maximum. The Stern–Volmer plot for both compounds is approximately linear, consistent with either a purely static or a purely dynamic fluorescence quenching process. Considering that, in average, the molecular lifetime of BSA in the absence of quencher is *ca.* 5 ns,[80, 81] a bimolecular rate constant of 5.97×10^{13} M^{-1}s^{-1} is obtained for **1** and 5.20×10^{13} M^{-1}s^{-1} for **2**. These values are well above the 2×10^{10} M^{-1}s^{-1} maximum value of the scattering collision quenching

View Article Online
DOI: 10.1039/D2DT00690A

constant for dynamic quenching,[80] which indicates mostly a static process for the quenching resulting from the interaction of the compounds with BSA.

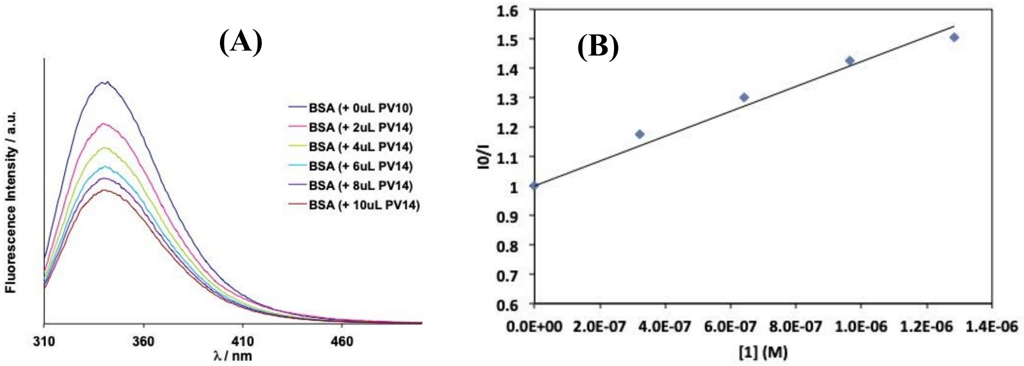

Fig. 4 Fluorescence emission spectra recorded at room temperature for solutions containing BSA (1.7 μM) and increasing amounts of **1** (0.3–1.6 μM) with λ_{exc} = 295 nm, in Hepes buffer 10 mM, pH 7.1. (B) Stern Volmer plot at λ_{em} = 342 nm (R^2 = 0.974). Note that in these dilute solutions, where the PV14 anions yield several distinct species whose relative concentrations change as they are progressively added, we do not expect good linearity in Stern Volmer plots.

Table 2 Steady-state fluorescence emission data for BSA-compound systems: quenching extent (%), Stern–Volmer constants (K_{SV}) and bimolecular rate constant (k_q) calculated for each compound.

Compound	Quenching (%)	log $(K_{SV})/M^{-1}$	λ_{em}^{max} /nm	$k_q/\mathrm{M}^{-1}\mathrm{s}^{-1}$
1	37	5.62	342	5.97×10^{13}
2	39	5.53	340	3.38×10^{13}

Interactions with ctDNA

Figures 5 and S21 (ESI) depict CD spectra of solutions containing ctDNA and compounds **2** and **1**, respectively.

View Article Online
DOI: 10.1039/D2DT00690A

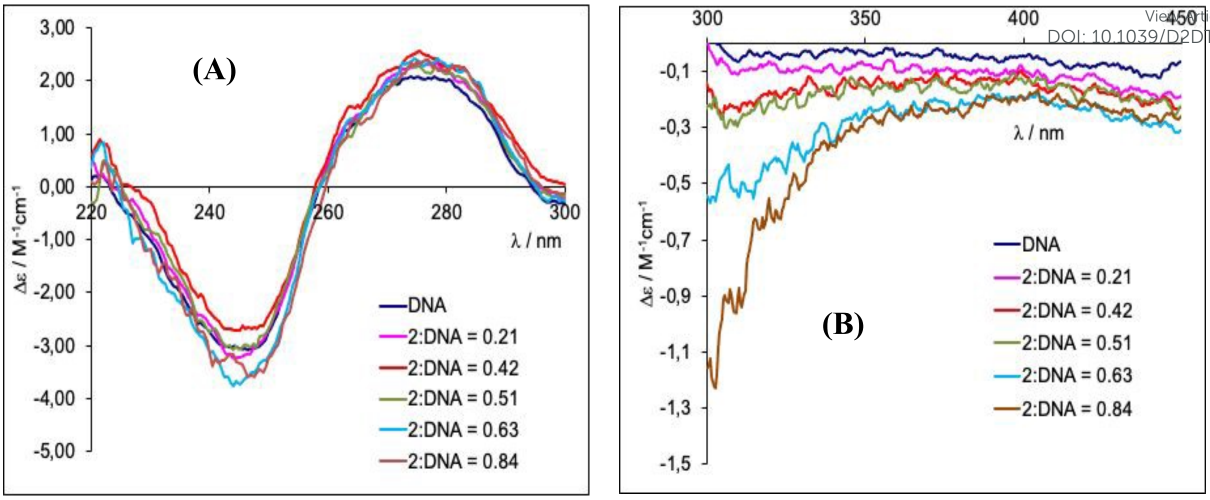

Fig. 5 CD spectra of solutions containing ctDNA in Hepes buffer (10 mM, pH = 7.1) and compound **2** (A) measured with a 5 mm optical path cell in the range 220-300 nm; (B) measured with a 20 mm optical path cell in the range 300-450 nm. The initial concentration of ctDNA was 61.2 μM nuc^{-1} and a solution of **2** with a concentration of 70.5 μM was progressively added.

In both cases some changes are seen in the CD spectra mainly for $\lambda > 300$ nm, particularly for higher relative amounts of PV14 compounds. CD spectra were similarly measured with solutions of methenamine and ctDNA (Fig. S22a) and 3-picoline and ctDNA (Fig. S22b). No significant changes could be seen in these cases, meaning that the changes observed in the CD spectra of Figs. 5 and S21 (ESI) are not due to the cations of compounds **1** and **2**. CD spectra were similarly measured with solutions of sodium vanadate (Fig. S23); besides an initial increase of molar ellipticity upon the first addition of $NaVO_3$ in the wavelength range of 230–300 nm ([V]:[ctDNA] = 0.22), no other changes are observed in the CD spectra of these solutions. This means that the changes observed in the CD spectra of Figs. 5 and S21 (ESI) are also not due to the formation of monovanadate (V_1, the most probable vanadate form at this pH and concentration), in the solutions used. Formation of vanadate-phosphate species cannot be ruled out.

Computational studies

Computational information allows us to have a deeper insight into the physicochemical properties of the systems, in combination with the experimental measurements. Since a few decades ago, Computational Transition Metal Chemistry has gained major influence among the chemical community largely due to the wide acceptance of density functional theory (DFT)-based methods.[82] The theoretical modelling of POMs is vast but still growing,[83] yet it has been shown that it is suitable for the understanding of a variety of questions such as the basicity of external oxygen sites,[84-88] the localization or delocalization of metal electrons in reduced species,[89, 90] the identification of host and guest subunits in a cage complex[91] and, more recently, questions as complex as their electrical conductivity,[92] and interaction of polyoxovanadates with proteins.[25] The DFT results herein presented describe the electronic structure of PV14, provide quantitative data about some of its fundamental properties, and somewhat predict how it may interact with other molecules.

For this purpose, we calculated structural parameters for the oxidized and one-electron reduced forms of $[PV_{14}O_{42}]^{9-}$ and $[H_4PV_{14}O_{42}]^{5-}$, namely some of their relevant interatomic distances, that can be found in Table 2. The values obtained are in general good agreement with the experimental characterization of the anions of **1** and **2**. It stands out the evolution of some distances with varying oxidation state (ox, red) or with the protonation state. In general, interatomic distance variations are minimal after reduction, as a consequence of the delocalization of the extra electron among practically all the V framework (see Fig. 6B). Some V–O_b distances suffer a maximal increase of 0.26 Å upon reduction but, in contrast, the rest of the tabulated values are nearly unaltered. Such a V–O_b distance change is attributed to the occupation of the Lowest Unoccupied Molecular Orbital (LUMO), which presents some d(V)-p(O) antibonding character. The effect of protonation on the tabulated distances can be considered also modest, as can be seen by comparison of the 1st and 4th numerical columns of Table 3.

Table 3 Computed structural parameters for the oxidized and one-electron reduced forms of $[PV_{14}O_{42}]^{9-}$ and $[H_4PV_{14}O_{42}]^{5-}$. All values are in Å.

	$PV_{14}O_{42}$	$PV_{14}O_{42}$-1e	$H_4PV_{14}O_{42}$	$H_4PV_{14}O_{42}$-1e
P–O_{tetr}	1.540	1.552	1.555–1.562	1.556–1.558
V–O_{term}	1.624–1.636	1.648–1.662	1.618–1.631	1.624–1.637
V_{cap}–O_b	1.779–1.942	1.824–1.921	1.848–1.931	1.850–1.981
V–O_b	1.750–2.103	1.783–2.375	1.735–2.138	1.721–2.120
V–O_{tetr}	2.373–2.383	2.375–2.406	2.389–2.443	2.378–2.458
Vcap–O_{tetr}	3.209	3.207	3.246	3.222–3.226
V–V_{cap}	3.003	3.033	2.993–3.014	2.947–3.067

View Article Online
DOI: 10.1039/D2DT00690A

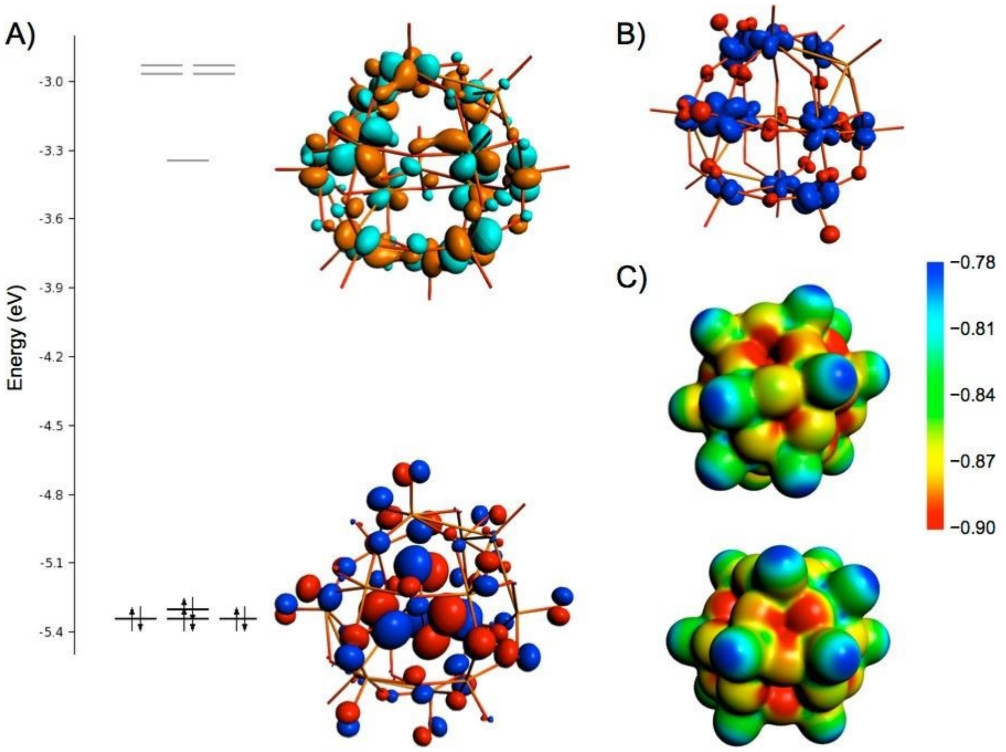

Fig. 6 Electronic properties of $[PV_{14}O_{42}]^{9-}$. A) Frontier molecular orbital energies and 3D representation of the HOMO and LUMO. B) 3D view of the spin density for the one-electron reduced system, $[PV_{14}O_{42}\ \text{-1e}]^{-10}$. Blue and red lobes represent excess spin α and excess spin β, respectively. C) MEP representation (two views) coloured by the potential value, with proton-attractor (nucleophilic) regions in red. Blue regions are less nucleophilic although, given the high negative charge of the molecule, it is expected that they still might attract cations.

We now examine some energetics of the oxidized system and the one-electron reduced counterpart. The fully deprotonated oxidized form, $[PV_{14}O_{42}]^{9-}$, obtained in conditions of aqueous solution, presents a Highest Occupied Molecular Orbital (HOMO) at –5.30 eV and a LUMO at –3.35 eV. Their energy difference, close to 2.00 eV, is typical of vanadium-based oxo clusters with d^0 metal centres. In comparison, tungsten-based classical POMs typically present much deeper HOMOs (as stable as –7.0 eV) and larger gaps, of the order of 2.5–2.8 eV.[93] In the present case, in line with most classical POM compounds, the HOMO is a combination of p(oxido) contributions of all the system, and the LUMO is a nonbonding combination of d(vanadium) contributions.[94] In the oxidized state, the molecular electrostatic potential (MEP), represented as a 3D-coloured surface, presents regions of higher nucleophilicity (red) at the bridging oxido sites. As usual in vanadium- and tungsten-based

View Article Online
DOI: 10.1039/D2DT00690A

POMs, terminal oxido positions present the lowest nucleophilicity (blue). Not all oxido sites present the same values of the electrostatic potential, therefore we infer that some are more easily protonated than others if the solution is a proton source. Fig. 7 collects the main facts presented above.

Following the experimental evidences about the possible protonation states of the system,[52, 58] we explored computationally the different protonated forms $[H_nPV_{14}O_{42}]^{(9-n)-}$, with $n = 1$–4. The protonation energies (PEs) of the different processes considered, formally expressed as

$$[H_nPV_{14}O_{42}]^{(9-n)-} + H_3O^+ \rightarrow [H_{(n+1)}PV_{14}O_{42}]^{(9-n-1)-} + H_2O$$

must vary with the degree of protonation of the reactant species. We used a value of –0.9807 eV for the proton release from the hydronium cation with the water cluster reaction $H_3O^+ + (H_2O)_{x-1} \rightarrow (H_2O)_x$. We started by comparing the first PEs, namely from the deprotonated to the mono- protonated species, at different oxygen sites of the framework. We considered as suitable for protonation bridging O-atoms only, since it is well known that terminal O-atoms of oxidovanadates are poorly basic.[88, 95] There are three main types of oxido sites (represented in Fig. 7) being site 1 the most basic, with PEs at sites 2 and 3 less exothermic by 2.04 and 6.10 kcal mol^{-1}, respectively. These energy differences correspond to larger pK_a values in site 2 by more than 1.2 units, and in site 3 by more than 4 units. With these results, we considered only protonation at site 1 as the dominant one. So, taking the oxidized species only, the first PE is –32.9 kcal mol^{-1}. The 2nd, 3rd and 4th protonations give smaller values, being the latter PE the smallest in the series, –21.4 kcal mol^{-1}. Interestingly, the differences in pK_a values reported by Selling *et al.*,[66] of 1.57 and 4.1, agree quite well with those obtained here.

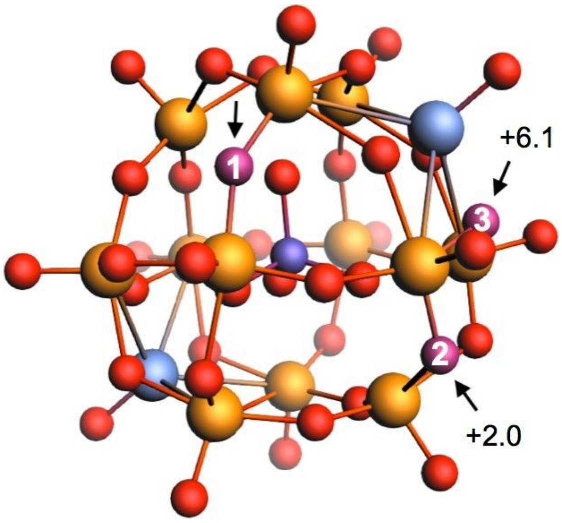

Fig. 7 Three types of bridging protonation sites considered for comparing the basicities for the $PV_{14}O_{42}$ system. PEs relative to position 1 are shown in kcal mol^{-1} (BP86 energies).

We also found important differences between the members of the series in terms of orbital energies and overall stability. In Fig. 8, a representation of the frontier orbital energies reveals that, as the degree of protonation increases, the orbitals are shifted down to lower energies by approximately 0.2 eV per proton. Particularly relevant are the LUMO energies, that go from –3.35 eV for the deprotonated form, to –4.53 eV for the H_4PV14 form. This is in line with the expected stabilization of the system due to the molecular charge reduction by one unit per added proton. The HOMO-LUMO gaps are all 0.3–0.4 eV smaller than that of the fully deprotonated form (1.55–1.68 vs 1.95 eV). These results clearly indicate that molecular reduction is energetically more favoured for protonated species.

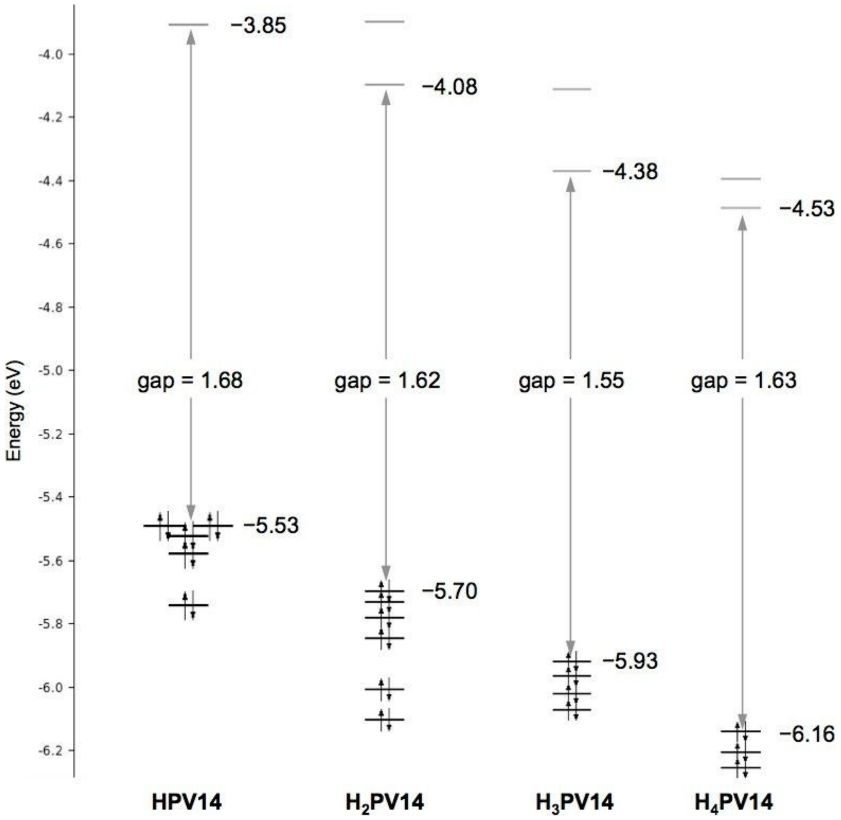

Fig. 8 Effect of protonation in orbital energies and overall stability. Schematic representation of the frontier molecular orbitals for the $[H_nPV_{14}O_{42}]^{(9-n)-}$ species. All the values are in eV. Horizontal lines stand for molecular orbital energies, and small arrows are electrons. The

View Article Online
DOI: 10.1039/D2DT00890A

HOMO-LUMO gap remains nearly unaltered. All the orbitals decrease monotonically as protons are added, in line with the total molecular charge decrease (from –8 to –5 from left to right).

The one-electron (1e) reduced species, in the absence of protonation, leads to the system with charge –10. This situation may be regarded as improbable due to the very high charge of the molecule. Despite that, the reduction energy is –3.34 eV. The extra electron is delocalized over the majority of the vanadium centres, four of them keeping a major fraction of it, and eight of them the rest of the electron (Fig. 6B). The two centres appearing as fully electron-depopulated are the capping ones which, in turn, do not contribute to the LUMO of the fully oxidized form. When reduction takes place on protonated forms, the computed REs are – 3.67, –3.83, –4.21 and –4.35 eV for the HPV14, H_2PV14, H_3PV14 and H_4PV14, respectively. In other words, if the 1e-reduction wave for the deprotonated form is arbitrarily located at 0.0 V, the corresponding waves for the mono-, di-, tri- and tetraprotonated derivatives are found at more positive potentials by ca. 0.33, 0.49, 0.87 and 1.02 V. Therefore, reduction of H_nPV14 will occur more easily (at less negative potentials) in acidic media approximately following this series of values. If there is more than one protonated species in equilibrium at a given pH, we will observe the reduction of the species in equilibrium with more protons. Calculations suggest that the degree of electron delocalization of the 1e-reduced system changes with the protonated state with, in general, a less delocalized electron than in the fully deprotonated form.

Combining protonation and reduction as a single process for each species, in general:

$$[H_nPV_{14}\,O_{42}]^{(9-n)-} + e^- + H_3O^+ \;\rightarrow\; [H_{(n+1)}PV_{14}\,O_{42}\,1e]^{(9-n)-} + H_2O$$

we find values of the order of –114 kcal mol^{-1} (–4.94 eV) for $n = 0$ to –122 kcal mol^{-1} (–5.28 eV) for $n = 2$ and 3. The main energy values related to the present study are listed in Table 4.

Table 4 Computed energies obtained from BP86 optimizations and OPBE single point runs.

	q^a	**Protonation Energy**		**H-L gap^b**		
		(eV)	(kcal mol^{-1})	(eV)		
PV_{14}	–9			1.95		
HPV_{14}	–8	–1.4283	–32.94	1.68		
H_2PV_{14}	–7	–1.0564	–24.36	1.62		
H_3PV_{14}	–6	–1.0669	–24.60	1.55		
H_4PV_{14}	–5	–0.9295	–21.43	1.63		

		Reduction Energy		Protonation Energy		**Prot. + Red. Energy**	
		(eV)	(kcal mol^{-1})	(eV)	(kcal mol^{-1})	(eV)	**(kcal mol^{-1})**
PV_{14} 1e	−10	−3.3369	−76.95				
HPV_{14} 1e	−9	−3.5092	−80.92	−1.601	−36.91	−4.937	**−113.9**
H_2PV_{14} 1e	−8	−3.8251	−88.21	−1.372	−31.65	−4.882	**−112.6**
H_3PV_{14} 1e	−7	−4.2107	−97.10	−1.452	−33.50	−5.278	**−121.7**
H_4PV_{14} 1e	**−6**	**−4.3548**	**−100.4**	**−1.074**	**−24.76**	**−5.284**	**−121.9**

[a] Total molecular charge. [b] HOMO-LUMO energy gap.

Conclusions

In this work, we report the synthesis and structure of two new bicapped Keggin phosphotetradecavanadate compounds $(C_6H_8N)_5[H_4PV_{14}O_{42}].5H_2O$ (**1**) and $(C_6H_{14}N_4)_2(NH_4)[H_4PV_{14}O_{42}]\cdot 11H_2O$ (**2**). These new polyoxometalate hybrid materials were characterized by elemental analysis, powder and single-crystal X-Ray diffraction, FT-IR, UV-Vis and ^{51}V, ^{31}P, ^{13}C and ^{1}H NMR spectroscopic methods.

Hirshfeld surface analyses, especially d_{norm} surface and fingerprint plots were used for decoding the intermolecular interactions topology in each crystal packing. Globally, although both hydrogen bonding and van der Waals interactions play relevant roles in the crystal packing of the two compounds, the O···H/H···O, O···O and H···H interactions are dominant. The results were supplemented with DFT calculations on the protonation and one electron reduction processes for $PV14^{9-}$ and H_4PV14^{5-} polyanions. The molecular electrostatic potential representations indicating that the proton-attracting (nucleophilic) regions are consistent with the results from the Hirshfeld surface data. We also found that reduction of the PV14 anions will occur more easily in acidic media. Interestingly, the estimates of differences in pK_a values of PV14 anions also agree quite well with those obtained experimentally.

We showed by circular dichroism and/or UV-Vis and/or fluorescence spectroscopy that the PV14 anions may interact with BSA and ctDNA. In biological experiments the pH is typically close to 7, and these media may contain several components that may bind POVs and/or the products of their decomposition. It is often reported that decavanadate POVs hydrolyse slowly at pH 7 and our data with PV14 anions suggest that these decompose faster than decavanadates; comparing equivalent media used in this work ~3-4 faster.

View Article Online
DOI: 10.1039/D2DT00690A

We must highlight that in biological experiments carried out with aqueous solutions of PV14 compounds, biological effects observed cannot be simply attributed to these POVs at the µM concentrations relevant in biological media. In fact, as evaluated by UV-Vis, the PV14 anions are not stable in aqueous solution at pH ~7, the hydrolysis proceeding faster as the total vanadium concentration decreases. At very low concentration of PV14 anions their hydrolysis yield several vanadium containing species, namely V_1 and V_2. In biologically relevant media, containing phosphate anions and other vanadium binders, the presence of vanadate-phosphate species as well as several types of complexes must be taken into account. Namely vanadium may bind to albumin and the types of species present also depend on the albumin:POV molar ratio. Therefore, when discussing the potential biological action of POVs all of potentially formed vanadium containing species must be considered.

Experimental section

Apparatus and reagents

3-picoline (Sigma), methenamine (Sigma), acetic acid, phosphoric acid (Sigma), sodium metavanadate (Sigma), ammonium vanadate and $CuSO_4\cdot5H_2O$ (Sigma) were used as provided. Millipore® water was used in all experiments with biological macromolecules. Calf-Thymus DNA and fatty acid free bovine serum albumin were purchased from Sigma-Aldrich. Other materials were of p.a. grade or equivalent.

Powder X-ray Diffraction pattern and CHN analyses support the compositions also determined from single-Crystal X-ray Diffraction crystal structure determinations. Elemental C, H and N analyses were done on a FISONS EA 1108 CHNS-O apparatus at *Laboratório de Análises* of *Instituto Superior Técnico*. The NMR spectra shown in Fig. 3 were recorded at ambient temperature on a Bruker Avance II + 500 (Ultra Shield TM Magnet) spectrometer operating at 500.13 MHz; most other experiments were carried out with a Bruker 400 MHz Avance II NMR spectrometer, 5 mm BBO probe. This equipment is permanently outfitted with a 5 mm two-channel Broad Band probe, allowing the observation of the following nuclei at the respective frequencies: ^{1}H, 400.0 MHz; ^{13}C, 100.58 MHz; ^{31}P, 161.924 MHz; ^{51}V, 105.152 MHz. Quartz tubes were used throughout the procedures. The ^{51}V NMR chemical shifts are reported in ppm using neat $V^{V}OCl_3$ in a capillary tube as reference. A glass capillary with 1 % H_3PO_4 in D_2O was used to standard the ^{31}P NMR signal. A drop of CD_3OD was used as ^{13}C NMR internal reference. The infrared spectra were recorded on an Alpha RT-DLaTGS HR 0.8 FTIR spectrometer and the UV-Visible absorption spectra were recorded on a Perkin Elmer Lambda

35 UV-Vis spectrophotometer with 10.0 or 2.0 mm optical path cuvettes. The thermogravimetric properties of the complexes (*ca.* 10-15 mg) were analyzed with a Perkin–Elmer simultaneous thermal analyser STA 6000 at a heating rate of 10 ºC min^{-1}, between 30 – 800 ºC, under a dinitrogen atmosphere (flow rate: 30 ml min^{-1}). Circular dichroism (CD) spectra were recorded on a Jasco J-720 spectropolarimeter. Fluorescence measurements were carried out on a SPEX® Fluorolog spectrofluorimeter (Horiba Jobin Yvon) in a FL3-11 configuration, equipped with a Xenon lamp using 10.0 mm quartz cuvettes. The instrumental response was corrected by means of a correction function provided by the manufacturer. The experiments were carried out at room temperature under gentle constant stirring and are all steady-state measurements.

Synthesis compound 1. To a solution of $NH_4V^VO_3$ (0.12 g, 1 mmol) in water (30 mL), $CuSO_4{\cdot}6H_2O$ (0.48 mg, 3 mmol) was added dropwise with constant stirring at room temperature in presence of five drops of H_3PO_4 (85%). At pH = 1.8, the solution turned deep maroon with time and the stirring was continued for *ca.* 5 h. Then 3-picoline (C_6H_7N) (0.03 mL, 0.3 mmol) was added slowly with stirring at room temperature. The reddish red maroon filtrate was allowed to evaporate at room temperature. The block, brown crystals of **1** suitable for X-ray diffraction were obtained within a few days. The yield is ca. 90% (based on V). Elemental analysis for $C_{30}H_{44}N_5PV_{14}O_{42}{\cdot}5H_2O$ (M_r = 1981 g.mol^{-1}): *Calc (%)*: C, 18.17; H, 2.72; N, 3.53; *Found (%)*: C, 18.01; H, 2.59; N, 3.94.

Synthesis compound 2. The synthetic procedure for compound **2** was similar to that of **1**, except that 1,3,5,7-Tetraazatricyclo[3.3.1.13,7]decane (Hexamethylenetetramine, metheamine, HMTA) (0.042 g, 0.3 mmol) was used instead of 3-picoline. Besides this, the evaporation time to obtain **2** was much shorter than that for **1**. Only one day later, red maroon block crystals were obtained. Yield: 80% (based on V). Elemental analysis for $C_{12}H_{36}N_9PV_{14}O_{42}{\cdot}11H_2O$ (M_r = 1920.8 g.mol^{-1}): *Calc*: C, 7.99; H, 1.83; N, 6.21 (%) *Found:* C, 7.72; H, 2.07; N, 6.53 (%).

Spectroscopic studies

DNA Interaction studies by Circular Dichroism Spectroscopy.

The CD experiments were done using ctDNA dissolved in aqueous Hepes buffer (10 mM, 150 mM NaCl and pH = 7.1). The measurements were done at ∼22 °C in a room with a controlled temperature using quartz Suprasil cells of 5.0, 10.0 or 20.0 mm optical path. The solutions of DNA, with concentrations varying in the range 55 to 85 μM, were prepared and left under

View Article Online
DOI: 10.1039/D2DT00690A

gentle stirring for ~1 h. Their exact concentrations were established by measuring the absorbance at 260 nm and taking $\varepsilon = 6600\ \mathrm{cm^{-1}M^{-1}}$.[75] Normally, accurately measured volumes of these solutions were transferred to a 5 and 20 nm optical path quartz cell, and accurately known volumes of solutions of compound **1** or **2** (with known concentrations) were added. After each addition, the sample was left with very gentle stirring inside the cell compartment of the CD apparatus for about 5-10 min, before the measurement of the spectrum.

The differential absorption values (ΔA values) measured correspond to $\Delta A = \Delta\varepsilon \times b \times C$, where b is the optical path, C is the total concentration of DNA, and $\Delta\varepsilon$ is ($\Delta\varepsilon = \varepsilon_L - \varepsilon_R$) the differential absorptivity per mole of DNA. Each CD spectrum is the result of 2 or 3 accumulations with a scan speed of 100 nm/min and a resolution of 0.5 nm. Once obtained it was processed with the Jasco 32 software available with the CD instrument and converted into Delta Epsilon ($\Delta\varepsilon$) values expressed in $\mathrm{M^{-1}cm^{-1}}$, taking the total concentration of DNA in the solution under consideration.

Stability studies by UV-Vis spectroscopy

The stability of compound **2** was evaluated by UV–Vis absorption spectroscopy in different concentrations in the absence and the presence of BSA. First, a stock solution of **2** was prepared in water with ca. 2 mM. Solutions were also prepared in Hepes buffer (pH ~7.0), having a final compound concentration of ca. 2, 5, 12, 20 and 100 μM (Fig S7a-d, ESI) and 49.1 μM (Fig S9, ESI). Also, a sample solution of BSA was prepared in the Hepes buffer (pH ~7) with a final concentration of 49.1 μM (Fig S8, ESI). Finally, a sample solution of compound **2** (49.1 μM) in the presence of BSA (99.8 μM) was prepared in Hepes buffer at pH = 7.0 (Fig S9, ESI). The UV−Visible spectra for all the solutions were recorded for a few hours and another was recorded after 24 h.

BSA binding by steady-state fluorescence spectroscopy

The interaction of BSA with the compounds was accessed by fluorescence emission spectroscopy using a 10×10 mm cell. Stock solutions of the compounds were prepared in water and used within a few hours. A solution of BSA with 1.7 μM for **1** and 1.5 μM for **2** concentrations was prepared directly in the quartz cuvette. Aliquots of the compounds’ stock solutions were then added to the cuvette to obtain the compound: protein ratios ranging from 0.19 to 0.94 for **1** and from 0.22 to 1.34 for **2**. In the experiments with 3-picoline and methenamine, the solutions inside the cell contained *ca.* 1.5 μM of BSA and additions of small amounts of each amine were done increasing its concentration in small steps up to final

View Article Online
DOI: 10.1039/D2DT00690A

amine/BSA ratios of 4.0 (methenamine) and 10.0 (3-picoline). All measurements were done in aqueous buffer 10 mM Hepes, 150 mM NaCl and pH 7.1. Part of the data obtained are in Figs. S17-S20 (ESI).

The fluorescence emission spectrum of each sample was measured by using the excitation wavelength at 295 nm and recording the emission spectrum in the 305–500 nm range. Baselines were recorded and subtracted from each sample fluorescence emission spectrum. Fluorescence emission intensity was corrected for the absorption and emission inner filter effects using the recorded UV-Vis absorption data of each sample.[80] The evaluation of the quenching of fluorescence emission of BSA by addition of solutions of **1** and **2** was done in steady-state conditions. The Stern–Volmer constant K_{SV}, a measure of the efficiency of the whole quenching process, is estimated for each system using the Stern–Volmer equation.[96]

$$I_0/I = 1 + k_q\tau_0[Q] = 1 + K_{SV}[Q]$$

Where I_0 and I are the fluorescence intensities in the absence and presence of quencher, respectively, corrected for reabsorption and inner filter effects,[80] k_q is the bimolecular quenching constant, τ_0 is the fluorophore average fluorescence lifetime, [Q] is the total quencher concentration and K_{SV} is the Stern-Volmer quenching constant.

Single-crystal X-ray crystallography. Crystallographic data for compounds **1** and **2** are summarized in Table S1 (ESI). Intensity data were collected at 100(2) K on an Agilent Technologies SuperNova diffractometer equipped with monochromated Mo Kα radiation (λ = 0.71073 Å) and an Eos CCD detector. Data frames were processed (unit cell determination, multiscan absorption correction, intensity data integration and correction for Lorentz and polarization effects) with CrysAlis Pro software package.[97] The structures were solved using OLEX2[98] program and refined by full-matrix least-squares using SHELXL-2018/9.[99]

Thermal vibrations for heavy (non-hydrogen) atoms were treated anisotropically. Some of the anisotropic thermal ellipsoids from POV oxygen atoms in **2** were normalized using ISOR-type restraints from SHELXL. Protonation sites from POV O-atoms in **1** were located in the Fourier map, in good agreement with BVS calculations. However, the worse quality of the data in **2** prevented us from locating these hydrogen atoms in the structural model. Hydrogen atoms of organic ligands were placed in calculated positions using standard SHELXL parameters. Compound **2** displays a significant disorder between lattice water molecules. Five positions suitable for hydration water molecules and half of ammonium molecule were located in the Fourier map. Their occupancies were initially refined without restrictions and fixed to the first

View Article Online
DOI: 10.1039/D2DT00690A

decimal in the last cycle, which result in a total number of 10 out of the expected 11 and one ammonium molecule. Hydrogen atoms belonging to hydration water molecules were placed in Fourier difference maps and O−H bond lengths were restrained to 0.87(2) Å. Crystal parameters and details of the data collection and refinement for the structures of **1** and **2** are listed in Table S1 (ESI). Molecular graphics are made with Diamond 3.2. CCDC 2145016 (compound **1**) and 2145017 (compound **2**) contain the supplementary crystallographic data for the structure reported in this paper. These data can be obtained free of charge via http://www.ccdc.cam.ac.uk/conts/retrieving.html, or from the Cambridge Crystallographic Data Centre, 12 Union Road, Cambridge CB2 1EZ, UK; fax: (+44) 1223 336 033; or e-mail: deposit@ccdc.cam.ac.uk. Supplementary data associated with this article may be found, in the online version, at doi: $$$$$.

Density Functional Theory calculations. Density functional theory (DFT) calculations were carried out on the series of $[H_nPV_{14}O_{42}]^{-9+n}$ derivatives, with n = 0–4. Within this series, the fully oxidized and one-electron reduced forms were also computed for every protonation state. For each derivative, a geometry optimization run was performed, and their energies, molecular orbitals and associated properties obtained. The calculations were carried out with the ADF 2019 program,[100] using triple-ξ + double polarization (TZ2P) basis sets for all atoms in combination with the frozen core approximation to the internal electrons of O (1s) , P (1s-2p) and V (1s-3p). The COSMO method was applied to mimic the effects of solvation of an aqueous solution (relative permittivity $\varepsilon = 78$). We applied the following density functionals of the generalized gradient approximation (GGA) family: BP86[101-103] for geometry optimizations and OPBE[104] for final energy single point runs. For open shell electronic configurations we applied the unrestricted formalism. It must be pointed out that optimization of the protonated forms can be especially intricate and the results presented here must be taken with moderate care. The possible orientations of hydrogen atoms attached to oxygen sites can lead to several local minima close in energy and, thus, the energetic analysis can suffer from slight inconsistencies. However, we think that the general conclusions presented are correct.

Abbreviations

BSA	Bovine serum albumin
BVS	Bond Valence Sum calculations
CD	Circular Dichroism

View Article Online
DOI: 10.1039/D2DT00690A

ctDNA	Calf Thymus DNA
de	distance from the point to the nearest nucleus external to the surface
di	distance to the nearest nucleus internal to the surface
DFT	Density Functional Theory
dnorm	normalized contact distance
δ_V	^{51}V NMR chemical shift
Hepes	4-(2-hydroxyethyl)-1-piperazineethanesulfonic acid
HTMA	methenamine, hexamethylenetetraamine
ID	distortion index
k_q	bimolecular rate constant
MEP	molecular electrostatic potential
PE	protonation energy
POM	Polyoxidometalate
POM	Polyoxidovanadate
PV_{14}	phosphotetradecavanadate
SC-XRD	single-crystal X-Ray diffraction
K_{SV}	Stern–Volmer constant
V_1	monovanadate
V_2	divanadate
V_4	tetravanadate
vdW	van der Waals radii

Conflicts of interest

There are no conflicts to declare.

Acknowledgements

This work was supported by Fundação para a Ciência e Tecnologia (FCT) (projects UIDB/00100/2020, UIDP/00100/2020 and LA/P/0056/2020) and by the Tunisian National Ministry of Higher Education and Scientific Research, an Agreement of Collaboration between the Faculty of science, University of Gabes-Tunisia and the Instituto Superior Técnico, University of Lisbon-Portugal. B.A. thanks Eusko Jaurlaritza/Gobierno Vasco (grants IT1291-19 and KK-2020/00008). N.R. acknowledges FCT for SFRH/BD/135797/2018 grant. X.L. acknowledges the grant PID2020-112762GB-I00 funded by the MCIN/AEI/

10.13039/501100011033. The Portuguese NMR of IST-UL are acknowledged for the access to the equipment.

References

1. M. T. Pope, *Heteropoly and Isopoly Oxometalates*, Springer, New York, 1983.
2. J. J. Borras-Almenar, E. Coronado, A. Muller and M. T. Pope, *Polyoxometalate Molecular Science*, Kluwer, Dordrecht, 2001.
3. D. L. Long, E. Burkholder and L. Cronin, *Chem. Soc. Rev.*, 2007, **36**, 105-121.
4. X. Huang, X. Gu, H. Zhang, G. Shen, S. Gong, B. Yang, Y. Wang and Y. Chen, *J. CO_2 Util.*, 2021, **45**, 101419.
5. A. Barbour, R. D. Luttrell, J. Choi, J. L. Musfeldt, D. Zipse, N. S. Dalal, D. W. Boukhvalov, V. V. Dobrovitski, M. I. Katsnelson, A. I. Lichtenstein, B. N. Harmon and P. Kogerler, *Phys. Rev. B: Condens. Matter. Mater. Phys.*, 2006, **74**, 014411.
6. J. Forster, B. Rosner, M. M. Khusniyarov and C. Streb, *Chem. Commun.*, 2011, **47**, 3114-3116.
7. Y. Kikukawa, K. Ogihara and Y. Hayashi, *Inorganics*, 2015, **3**, 295-308.
8. X.-M. Lin, X.-D. Feng, Y. Wang, Y.-H. Xing, L.-X. Sun, S.-Y. Wei and Z. S. Z., *J. Coord. Chem.*, 2017, **70**, 44-59.
9. R. Weinstock, R. E. Schreiber and R. Neumann, *Chem. Rev.*, 2018, **118**, 2680-2717.
10. J. X. Liu, X. B. Bang, Y. L. Li, S. L. Huang and G. Y. Yang, *Coord. Chem. Rev.*, 2020, **414**, 213260.
11. J. Li, C. Wei, Y. Han, Y. Mei, X. Cheng, X. Huang and C. Hu, *Dalton Trans.*, 2021, **50**, 10082-10091.
12. J. S. Qin, D. Y. Du, W. Guan, X. J. Bo, Y.-F. Li, L. P. Guo, Z. M. Su, Y. Y. Wang, Y. Q. Lan and H. C. Zhou, *J. Am. Chem. Soc.*, 2015, **137**, 7169-7177.
13. C. Wang, Z. Xie, K. E. deKrafft and W. Lin, *J. Am. Chem. Soc.*, 2011, **133**, 13445-13454.
14. L. E. VanGelder, T. R. Cook and E. M. Matson, *Comm. Inorg. Chem.*, 2019, **39**, 51-89.
15. H. N. Miras, L. Vilà-Nadal and L. Cronin, *Chem. Soc. Rev.* , 2014, **43**, 5679–5699.
16. H. Morita, R. Tsunashima, S. Nishihara, K. Inoue, Y. Omura, Y. Suzuki, J. Kawamata, N. Hoshino and T. Akutagawa, *Angew. Chem. Int. Ed.*, 2019, **58**, 9184–9187.
17. D. Rehder, *Bioinorganic Vanadium Chemistry*, John Wiley & Sons, Ltd., Chichester, 2008.
18. J. O. E. Nriagu, *Vanadium in the Environment*, John Wiley & Sons, New York, 1998.
19. A. Bijelic, M. Aureliano and A. Rompel, *Angew. Chem. Int. Ed.*, 2019, **58**, 2980-2999.
20. J. T. Rhule and C. L. Hill, Judd, D.A., *Chem. Rev.*, 1998, **98**, 327-357.
21. N. I. Gumerova and A. Rompel, *Chem. Soc. Rev.*, 2020, **49**, 7568-7601.
22. N. Samart, D. Althumairy, D. Zhang, D. A. Roess and D. C. Crans, *Coord. Chem. Rev.*, 2020, **416**, 213286.
23. N. I. Gumerova and A. Rompel, *Inorg. Chem.*, 2021, **60**, 6109−6114.

View Article Online
DOI: 10.1039/D2DT00690A

24. M. Aureliano, N. I. Gumerova, G. Sciortino, E. Garribba, A. Rompel and D. C. Crans, *Coord. Chem. Rev.*, 2021, **447**, 214143.

25. M. Aureliano, N. I. Gumerova, G. Sciortino, E. Garribba, C. C. McLauchlan, A. Rompel and D. C. Crans, *Coord. Chem. Rev.*, 2022, **454**, 214344.

26. O. Linnenberg, M. Moors, A. Notario-Estévez, X. López, C. de Graaf, S. Peter, C. Baeumer, R. Waser and K. Y. Monakhov, *J. Am. Chem. Soc.* , 2018, **140**, 16635-16640.

27. M. Moors, J. Warneke, X. López, C. de Graaf, B. Abel and K. Y. Monakhov, *Acc. Chem. Res.*, 2021, **54**, 3377-3389.

28. M. O. Keeffe and O. M. Yaghi, *Chem. Rev.*, 2012, **112**, 675-702.

29. I. Andersson, A. Gorzsas, C. Kerezsi, I. Tóth and L. Pettersson, *Dalton Trans.*, 2005, 3658-3666.

30. H. Hayashi, *Coord. Chem. Rev.*, 2011, **255**, 2270-2280.

31. C. Streb, in *Polyoxometalate-Based Assemblies and Functional Materials*, ed. Y.-F. Song, Springer, Cham, 2017, vol. 176, pp. 31-47.

32. R. L. Meyer, R. Love, W. W. Brennessel and E. M. Matson, *Chem. Commun.*, 2020, **56**, 8607-8610.

33. Y. Kikukawa, K. Seto, S. Uchida, S. Kuwajima and Y. Hayashi, *Angew. Chem. Int. Ed.*, 2018, **57**, 16051-16055.

34. M. Aureliano and D. C. Crans, *J. Inorg. Biochem.*, 2009, **103**, 536-546.

35. D. C. Crans, J. J. Smee, E. Gaidamauskas and L. Yang, *Chem. Rev.*, 2004, **104**, 849-902.

36. M. Aureliano, G. Fraqueza and C. A. Ohlin, *Dalton T*, 2013, **42**, 11770-11777.

37. L. C. Cantley, L. Josephson, R. Warner, M. Yanagisawa, C. Lechene and G. Guidotti, *J. Biol. Chem.*, 1977, **252**, 7421–7423.

38. J. C. Pessoa, S. Etcheverry and D. Gambino, *Coord. Chem. Rev.*, 2015, **301**, 24-48.

39. J. C. Pessoa, E. Garribba, M. F. A. Santos and T. Santos-Silva, *Coord. Chem. Rev.*, 2015, **301**, 49-86.

40. J. Costa Pessoa, M. F. A. Santos, I. Correia, D. Sanna, G. Sciortino and E. Garribba, *Coord. Chem. Rev.*, 2021, 214192.

41. L. C. Cantley, L. G. Cantley and L. Josephson, *J. Biol. Chem.*, 1978, **253**, 7361-7368.

42. L. C. Cantley, J. H. Ferguson and K. Kustin, *J. Am. Chem Soc.*, 1978, **100**, 5210-5212.

43. M. B. Čolović, D. V. Bajuk-Bogdanović, N. S. Avramović, I. D. Holclajtner-Antunović, N. S. Bošnjaković-Pavlović, V. V.M. and D. Z. Krstić, *Bioorg. Med. Chem.*, 2011, **19**, 7063-7069.

44. G. Fraqueza, C. A. Ohlin, W. H. Casey and M. Aureliano, *J. Inorg. Biochem.*, 2012, **107**, 82-89.

45. D. W. Boyd, K. Kustin and M. Niw, *Biochim. Biophys. Acta (BBA) Protein Struct. Mol. Enzymol.*, 1985, **827**, 472-475.

46. M. P. M. Marques, D. Gianolio, S. Ramos, L. A. E. Batista de Carvalho and M. Aureliano, *Inorg. Chem.*, 2017, **56**, 10893-10903.

47. Y. Chujo, *KONA Powder Particle J.*, 2007, **25**, 255-260.

48. G. Kickelbick, *Hybrid Materials*, Wiley-VCH Verlag, Wemheim, 2006.

49. J. K. Li, C. P. Wei, D. G. J. Guo, C. C. Wang, Y. F. Han, G. F. He, J. P. Zhang, X. Q. Huang and C. W. Hu, *Dalton Trans.*, 2020, **49**, 14148-14157.

View Article Online
DOI: 10.1039/D2DT00690A

50. X. Q. Huang, Y. Q. Qi, Y. X. Gu, S. W. Gong, G. D. Shen, Q. Li and J. K. Li, *Dalton Trans.*, 2021, **49**, 10970-10976.

51. K. Y. Monakhov, W. Bensch and P. Kögerler, *Chem. Soc. Rev.*, 2015, **44**, 8443-8483.

52. M. I. Khan, J. Zubieta and T. P., *Inorg. Chim. Acta*, 1992, **193**, 17-20.

53. M. Grabau, J. Forster, K. Heussner and C. Streb, *Eur. J. Inorg. Chem.*, 2011, **2011**, 1719-1724.

54. H. T. Evans Jr. and M. T. Pope, *Inorg. Chem.*, 1984, **23**, 501-504.

55. W. H. Baur, *Acta Crystallogr.*, 1974, **B30**, 1195-1215.

56. I. D. Brown and D. Altermatt, *Acta Crystallogr. B*, 1985, **41**, 244-247.

57. A. García-García, L. Noriega, F. J. Meléndez-Bustamante, M. E. Castro, B. L. Sánchez-Gaytán, D. Choquesillo-Lazarte, E. González-Vergara and A. Rodríguez-Diéguez, *Inorganics*, 2021, **9**, 67.

58. G. Fraqueza, J. Fuentes, L. Krivosudský, S. Dutta, S. S. Mal, A. Roller, G. Giester, A. Rompel and M. Aureliano, *J. Inorg. Biochem.*, 2019, **197**, 110700.

59. K. Nomiya, K. Kato and M. Miwa, *Polyhedron*, 1986, **5**, 811-813.

60. Z. S. Peng, Y.-L. Huang, S. Z. Lü, J.-T. Tang, T.-J. Cai and Q. Deng, in *Synthesis and Reactivity in Inorganic, Metal-Organic, and Nano-Metal Chemistry*, Taylor & Francis, 2014, vol. 44, pp. 376-382.

61. T. Ramachandramoorthy, A. P. Raj, V. Sivasankar and S. Rajam, *Asian J. Chem.*, 2007, **19**, 4415-4419.

62. Z. Yi, X. Yu, W. Xia, L. Zhao, C. Yang, Q. Chen, X. L. Wang, X. Xu and X. Zang, *CrystEngComm*, 2010, **12**, 242-249.

63. K. Ezzayani, A. B. Khelifa, E. Saint-Aman, F. Loiseau and H. Nasri, *J. Mol. Struct.*, 2017, **1137**, 412-418.

64. *Microcal Origin Version 8.0, Microcal Software Inc. One, Northampton* 2009.

65. S. P. Gerhardt, J. N. Talmadge, J. M. Canik and D. T. Anderson, *Physics Plasmas*, 2005, **12**, 056116.

66. A. Selling, I. Andersson, L. Pettersson, C. M. Schramm, S. L. Downey and J. H. Grate, *Inorg. Chem.*, 1994, **33**, 3141–3150.

67. J. Friedl, M. V. Holland-Cunz, F. Cording, F. Pfanschilling, C. Wills, W. McFarlane, B. Schricker, R. Fleck, H. Wolfschmidt and U. Stimming, *Energy Environ. Sci.*, 2018, **11**, 3010-3018.

68. T. Ueda, Y. Nishimoto, R. Saito, M. Ohnishi and J.-I. Nambu, *Inorganics*, 2015 **3**, 355-369.

69. M. Pascual-Borràs, X. López and J. M. Poblet, *Phys. Chem. Chem. Phys.*, 2015, **17**, 8723-8731.

70. T. Jakusch, A. Dean, T. Oncsik, A. C. Bényei, V. Di Marco and T. Kiss, *Dalton Trans.*, 2010, **39**, 212-220.

71. M. A. Spackman and J. J. McKinnon, *CrystEngComm*, 2002, **4**, 378-392.

72. M. A. Spackman and D. Jayatilaka, *CrystEngComm*, 2009, **11**, 19-32.

73. F. L. Hirshfeld, *Theor. Chim. Acta*, 1977, **44**, 129-138.

74. X. M. He and D. C. Carter, *Nature*, 1992, **358**, 209-215.

75. F. W. Putnam, *The Plasma Proteins*, Academic Press, New York, 1984.

View Article Online
DOI: 10.1039/D2DT00690A

76. D. C. Carter and J. Ho, *Adv. Protein Chem.*, 1994, 153-203.

77. W. Bal, J. Christodoulou, P. J. Sadler and A. Tucker, *J Inorg Biochem*, 1998, **70**, 33-39.

78. J. Ghuman, P. A. Zunszain, I. Petitpas, A. A. Bhattacharya, M. Otagiri and S. Curry, *J. Mol. Biol.*, 2005, **353**, 38-52.

79. N. Tayeh, T. Rungassamy and J. R. Albani, *J. Pharm. Biom. Anal.*, 2009, **50**, 107-116.

80. J. R. Lakowicz, *Principles of fluorescence spectroscopy*, Springer, Boston, MA, 3rd edn., 2006.

81. N. Ribeiro, R. E. Di Paolo, A. M. Galvão, F. Marques, J. C. Pessoa and I. Correia, *Spectrochim. Acta A*, 2018, **204**, 317-327.

82. E. R. Davidson, *Chem. Rev.*, 2000, **100**, 351-352.

83. X. López, J. J. Carbó, C. Bo and J. M. Poblet, *Chem. Soc. Rev.*, 2012, **41**, 7537-7571.

84. J. Y. Kempf, M.-M. Rohmer, J.-M. Poblet, C. Bo and M. Bénard, *J. Am. Chem. Soc.*, 1992, **114**, 1136-1146.

85. J. M. Maestre, J. P. Sarasa, C. Bo and J.-M. Poblet, *Inorg. Chem.*, 1998, **37**.

86. J. M. Poblet, X. López and C. Bo, *Chem. Soc. Rev.*, 2003, **32**, 297-308.

87. J. A. Fernández, X. López and J. M. Poblet, *J. Mol. Catal A: Chem.*, 2007, **262**, 236–242.

88. N. Bošnjakovic-Pavlović, A. Spasojević-de Biré, I. Tomaz, N. Bouhmaida, F. Avecilla, U. Mioč, J. C. Costa Pessoa and N. E. Ghermani, *Inorg. Chem.*, 2009, **48**, 9742-9753.

89. L. Parent, P. A. Aparicio, P. Oliveira, A.-L. Teillout, J. M. Poblet, X. López and I. M. Mbomekallé, *Inorg. Chem.*, 2014, **53**, 5941-5949.

90. E. R. W. Salomon, X. López, N. Suaud, P. Mialane, M. Haouas, A. Saad, J. Marrot and A. Dolbecq, Dalton Trans. 2018, 47, 10636-10645, *Dalton Trans.*, 2018, **47**, 10636-10645.

91. M.-M. Rohmer, J. Devemy, R. Wiest and M. Bénard, *J. Am. Chem. Soc.*, 1996, **118**, 13007-13014.

92. A. Notario-Estévez, X. López and C. de Graaf, *Dalton Trans.*, 2021, **50**, 5540-5551.

93. X. López, J. M. Maestre, C. Bo and J. M. Poblet, *J. Am. Chem. Soc.*, 2001, **123**, 9571-9576.

94. A. S. Daura, A. Notario-Estévez, J. J. Carbó, J. M. Poblet, C. de Graaf, K. Y. Monakhov and X. López, *Inorg. Chem.*, 2019, **58**, 3881-3894.

95. W. G. Klemperer and W. Shum, *Angew. Chem. Int. Ed. Engl.*, 1977, **15**, 3544-3545.

96. V. B. and M. N. Berberan-Santos, *Molecular Fluorescence: Principles and Applications*, John Wiley & Sons, 2 edn., 2012.

97. *CrysAlisPro Software System, Version 171.37.34; Agilent Technologies UK Ltd.: Oxford, UK*, 2012.

98. O. V. Dolomanov, L. J. Bourhis, R. J. Gildea, J. A. K. Howard and H. Puschmann, *J. Appl. Crystallogr.*, 2009, **42**, 339-341.

99. G. M. Sheldrick, *Shelxl-2018, Program for the Crystal Structure refinement; University of Göttingen: Göttingen, Germany*, 2018.

100. G. Te Velde, F. M. Bickelhaupt, S. J. A. van Gisbergen, C. Fonseca Guerra, E. J. Baerends, J. G. Snijders and T. Ziegler, *J. Comput. Chem.*, 2001, **22**, 931-967.

101. J. P. Perdew, *Phys. Rev. B: Condens. Matter Mater. Phys.*, 1986, **33**, 8822-8824.

102. J. P. Perdew, *Phys. Rev. B: Condens. Matter Mater. Phys.*, 1986, **34**, 7406.

103. A. D. Becke, *Phys. Rev. A: At., Mol., Opt. Phys.*, 1988, **38**, 3098-3100.

104. N. C. Handy and A. J. Cohen, *Mol. Phys.*, 2001, **99**, 403-412.

View Article Online
DOI: 10.1039/D2DT00690A